Logistic splicing correction for VNIR-SWIR reflectance imaging spectroscopy

FEDERICO GRILLINI[1,*], JEAN-BAPTISTE THOMAS[1,2], AND SONY GEORGE[1]

[1] Colourlab, Norwegian University of Science and Technology (NTNU), Norway
[2] ImViA Laboratory, University of Burgundy, France
[*] Corresponding author: federico.grillini@ntnu.no

Compiled December 4, 2023

In the field of spectroscopy, a splicing correction is a process by which two spectra captured with different sensors in adjacent or overlapping electromagnetic spectrum ranges are smoothly connected. In our study we extend this concept to the case of reflectance imaging spectroscopy in the visible-near infrared (VNIR) and short-wave infrared (SWIR), accounting for additional sources of noise that arise at the pixel level. The proposed approach exploits the adaptive fitting of a logistic function to compute correcting coefficients that harmonize the two spectral sets. This short letter addresses usage conditions and compares results against the existing state of the art.

http://dx.doi.org/10.1364/ao.XX.XXXXXX

In recent years many fields of research have experienced the deployment of reflectance imaging spectroscopy (RIS, also commonly known as hyperspectral imaging), often simultaneously combining the performances of imagers in the visible (VIS), near-infrared (NIR), and short-wave-infrared (SWIR) regions of the electromagnetic spectrum [1–5]. Albeit two different spectral sensors may capture the same physical quantity, namely spectral radiance, the reported values will hardly match if compared at corresponding wavelengths. The difference in response, which upon visual observation of two complementary spectra results in what has been defined in the literature as a "radiometric jump", "stepped data" or "spectral discontinuity", arises from a variety of factors that have been extensively studied by manufacturers in the field of spectroscopy [6, 7]. In [8], it was identified that the detector responsible for the observation of visible light was largely affected by warm-up time causing spectral sensitivity drift. In [7] the authors model the behavior of the VNIR sensor as a function of ambient temperature, while they find that the response of the infrared detector was not affected. One of the main reasons for the presence of discontinuities is the decreasing signal-to-noise ratio (SNR) at the extremities of the sensitive regions of the semiconductor materials from which the detectors are built: indeed, the absorption coefficients of the most commonly used semiconductors rarely overlap [9], making it hard to obtain a reliable combination of sensors in a wide range of wavelengths. For example, silicon (Si), the most used material to detect visible radiation, ends its operational range at around 1000 nm [10]. Materials such as Indium-Gallium-Arsenide (InGaAs) and Mercury-Cadmium-Telluride (HgCdTe) are used to detect infrared radiation, but need to be accurately designed (with an intrinsic concentration of elements) and appropriately cooled to be able to sense radiation at about 1000 nm [11]. Another factor that possibly generates jumps is the switch in bandwidth between two adjacent sensors, which leads to a different amount of energy incoming on the detectors, even for the same nominal wavelength.

Solutions to the problem of radiometric jumps are often referred to in the spectroscopy literature as "splicing correction" and include additive, multiplicative [12] and parabolic correction routines [13]. While the former two make use of a global correction scalar or coefficient, the latter solution proposes a wavelength-dependent coefficient to erase the radiometric jump by matching one spectrum to the other. In [7] the authors state that multiplicative and additive corrections lead to the introduction of more errors in the spectra, especially when considering high-energy spectra, while the parabolic method efficiently matches jumps up to a 6% difference, but struggles to correct larger spectral discrepancies.

In VNIR-SWIR RIS, although observed [14], the problem has not been deeply studied by the community. In remote sensing and airborne applications the bands around 970 nm are sometimes not processed due to the presence of a water absorption band [15], while with the motivation of low SNR, it is commonly accepted for laboratory applications to discard such flawed spectral bands and conduct further steps of analysis on disconnected or independent image datasets [1]. However, there is a need to preserve as much as possible of the available information to enhance visualization methods and to be able to highlight important spectral signatures in the interval of wavelengths that could be lost. When an imaging application is considered against a spectroscopy one, it is necessary to extend the list of factors that generate spectral discrepancies at the pixel level. First of all, the magnitude of the jumps is highly influenced by the performances of image registration, especially in the case in which the two images have different (x, y) dimensions and a scale difference exists. In this case, despite the fact that sub-pixel accuracy can be achieved, the perfect pixel correspondence is an ideal condition. Moreover, reproducing the exact same relative positioning of object-illumination-camera is a rather difficult task when two separate imagers are deployed in an environment that can be adjusted only manually, and spurious differences in Bidirectional Reflectance Distribution Function (BRDF) [16] at the pixel level may generate a small difference in response.

The authors in [17] adapt the parabolic correction routine to concatenate VNIR and SWIR hyperspectral images of airborne sensing. In our previous attempt [18], global coefficients were learned through the optimization of a joint radiometric correction performed on standardized targets, but the results could not correctly generalize in terms of spectral variability and jump magnitude.

We propose a new adaptive splicing correction routine for complementary hyperspectral images that share an overlap of nominal wavelengths. Furthermore, we propose an evaluation that compares the results obtained with the proposed solution against the state of the art represented by the parabolic splicing correction. In this specific case, we consider a laboratory use of dual RIS in the VNIR and SWIR regions, deploying push-broom hyperspectral imagers manufactured by Hyspex (NEO, Norway), for which the main specifications are reported in Table 1. Upon inspection of the data, it is noticeable that the spectral ranges overlap in the region between 950 nm and 1000 nm with 16 and 9 bands for VNIR and SWIR respectively. The pre-processing of the images includes radiometric calibration and co-registration, adopting the methodology proposed in [19] and following the guidelines highlighted in one of our previous studies [20].

Name	VNIR	SWIR
Sensor	Si (CMOS)	HgCdTe
Cooling	NA	150 K
Spatial lines	1800	384
Spectral range [nm]	$400-1000$	$1000-2500$
FWHM [nm]	3.26	5.45

Table 1. Technical specifications of VNIR1800 and SWIR384 hyperspectral imagers.

The laboratory conditions of the set-up accentuate possible differences in BRDF due to the manual positioning of the illumination sources and the hyperspectral imagers. Thus, the experimental set-up (schematically reported in Figure 1) must be designed in a way that respects as much as possible the same illumination geometry for the two imagers. This also implies that the cameras are carefully aligned, both to maximize the overlap of the fields of view and to reduce pixel-wise differences of the BRDF. Furthermore, it will be necessary to calibrate the scene radiance captured by the two cameras and move into an illumination-independent space (absolute spectral reflectance), as there might be differences in the spectral power distribution (SPD) of the deployed illumination sources as well.

Let $\mathbf{F}(x, y, \lambda)$ be a spectral image defined in the image domain $\mathcal{D}$ with spatial coordinates (x, y) and spectral sampling in correspondence of wavelengths $\lambda \in \Lambda$. Generally, Λ is defined in $[\lambda_{min}, \lambda_{max}]$, but in our specific case it is the result of two separate image capture processes that generate

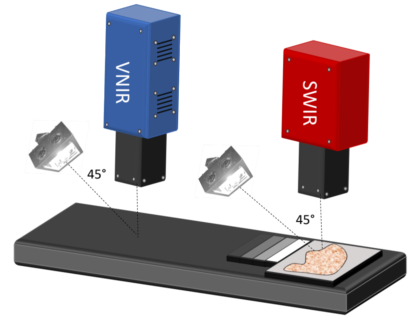

Fig. 1. Acquisition set-up of simultaneous push-broom VNIR-SWIR RIS. The illumination geometry (45/0) is carefully adjusted for both imagers. However, differences in SPD of the individual light source may exist.

$\mathbf{V}(x, y, \lambda_v)$ with $\lambda_v \in \Lambda_v$, $\Lambda_v = [400, 1000]\, nm$ and $\mathbf{S}(x, y, \lambda_s)$ with $\lambda_s \in \Lambda_s$, $\Lambda_s = [1000, 2500]\, nm$. Therefore, there exists a shared interval of wavelengths $\Lambda' = \Lambda_v \cap \Lambda_s$. Assuming that $\mathbf{V}$ and $\mathbf{S}$ are spatially co-registered and equally sampled in Λ', we can define $\mathbf{V}'(\lambda')$ and $\mathbf{S}'(\lambda')$. We aim at finding the transform $\mathcal{T}$ that associates (dropping the spatial coordinates for readability):

$$\mathbf{F}(\lambda) = \mathcal{T}\left(\mathbf{V}(\lambda_v), \mathbf{S}(\lambda_s)\right) \tag{1}$$

For each image it is also possible to define the set of bands that lie outside of the overlapping range as $\Lambda_v'' = \Lambda_v \setminus \Lambda'$ and $\Lambda_s'' = \Lambda_s \setminus \Lambda'$, associated to the *truncated* spectral images $\mathbf{V}''(\lambda_v'')$ and $\mathbf{S}''(\lambda_s'')$.

The region in which $\mathbf{V}'$ and $\mathbf{S}'$ lie is where the radiometric jumps take place. Because of the aforementioned noise sources (different bandwidth, decreasing SNR, differences in BRDF, and sub-pixel misregistration), we assume that neither of the overlapping sets is a reliable estimate of the final spectrum. For this reason, we decide that a possible correct position could be the mean between $\mathbf{V}'$ and $\mathbf{S}'$, noticing that this observation can be adjusted based on specific priors.

$$\mathbf{R} = \frac{1}{2}\left(\mathbf{V}' + \mathbf{S}'\right) \tag{2}$$

Then we can define correcting coefficients Φ_v' and Φ_s' for VNIR and SWIR, valid in the overlapping region, such as

$$\mathbf{R} = \Phi_v' \mathbf{V}' = \Phi_s' \mathbf{S}' \tag{3}$$

When using the mean value as a reference for matching, the correcting coefficients will be found symmetrically distributed around 1. Ideally, the spliced spectrum should preserve the shapes of the original spectra and also match their magnitude values at some points away from the overlapping range. In order to do so, the correcting coefficients should smoothly vary from the values of Φ_v' and Φ_s' to 1. We achieve this by deploying a logistic function. In such a distribution, three parameters must be defined: the maximum value L, the slope k, and the center of the distribution x_0.

In this specific case, L is either the unity value or the coefficient at the extreme of the overlapping range: $\varphi_v \in \Phi_v'$ (first coefficient) and $\varphi_s \in \Phi_s'$ (last coefficient), while k and x_0 are determined as a function of the distance Δr between $\mathbf{V}'$ and $\mathbf{S}'$:

$$\Delta r = \sqrt{\frac{1}{N'} \sum_{i=1}^{N'} \left(\mathbf{V}' - \mathbf{S}'\right)^2} \tag{4}$$

in which N' is the number of bands in the overlapping range. In typical VNIR-SWIR applications, the values of Δr follow the probability density function depicted in Figure 2. Here we can observe that a value of 6% can already be considered very large.

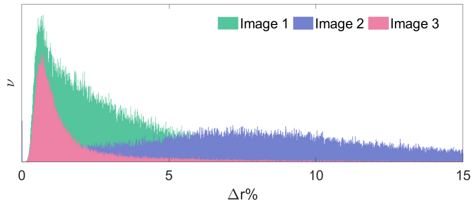

Fig. 2. Typical relative spectral discrepancy histograms stemming from three hyperspectral images.

The center of the logistic curve x_0 is intrinsically linked to the width of the spectral window that will experience the correction, as it is the median value of the selected interval. Therefore, λ_0 is obtained indirectly from the modeling of the window width w. To obtain smoothly connected spectra it is desirable to have a steeper slope (higher k) and a low w (number of spectral bands affected by the correction) when the value of Δr is small, and vice versa. The window width w is modeled as a logistic function of the form:

$$\begin{aligned} w_v &= \frac{N''_v}{1 + exp\left[-c_v\left(\Delta r - x_{0v}\right)\right]} \\ w_s &= \frac{N''_s}{1 + exp\left[-c_s\left(\Delta r - x_{0s}\right)\right]} \end{aligned} \quad (5)$$

in which N''_v and N''_s represent the number of bands in Λ''_v and Λ''_s respectively. The parameters c_v, c_s, x_{0v}, and x_{0s} are learned by fitting the logistic function to the logarithmically spaced values of Δr, in an interval that can be case-specific (in the case of correction of pair of spectra) or empirically learned from the Δr distribution (in the case images and large spectral libraries). We can now define $\Lambda'''_v \subset \Lambda''_v$ and $\Lambda'''_s \subset \Lambda''_s$ as the subsets that experience the splicing correction with a number of bands equal to w_v and w_s, respectively. The central wavelengths λ_{0v} and λ_{0s} are then the median values of such intervals.

The slope k_v of the VNIR range can be found as the exponential function:

$$k_v = a \cdot exp\left(b\Delta r\right) + y \quad (6)$$

in which the parameters a, b, and y are retrieved by fitting the function to a linear vector decreasing from 1 to 0. We note here that if the modeling is performed in the same way for the SWIR counterpart, the normalization in [0,1] brings the fits of k_v and k_s to match. However, we can use prior information to model k_s so that it generates a flatter logistic curve since the affected wavelength interval is larger.

$$k_s = k_v \frac{N''_v}{N''_s} \quad (7)$$

The correction coefficients in Λ''_v and Λ''_s can now be determined as:

$$\begin{aligned} \psi_v(\lambda''_v) &= \frac{sgn(\varphi_v - \varphi_s)}{1 + exp\left[-k_v\left(\lambda''_v - \lambda_{0v}\right)\right]}\left|\varphi_v - 1\right| + 1 \\ \psi_s(\lambda''_s) &= \frac{sgn(\varphi_v - \varphi_s)}{1 + exp\left[-k_s\left(\lambda''_s - \lambda_{0s}\right)\right]}\left|\varphi_s - 1\right| + \varphi_s \end{aligned} \quad (8)$$

The full, smoothly connected hyperspectral image is obtained by concatenating along the spectral dimension (dropping the λ-dependency for readability):

$$\mathbf{F} = \left[\mathbf{V}'' \cdot \Psi_v\,,\, \mathbf{R}\,,\, \mathbf{S}'' \cdot \Psi_s\right] \quad (9)$$

An example of splicing correction on measured spectra can be found in Figure S1 in Supplement 1.

The problem of spectral splicing has infinite solutions, as two spectra can be connected and modified in infinite ways, but only a limited set of pertinent solutions. Thus, the evaluation of the final spectrum and the validation of the methodology can be tricky. In order to help the evaluation, a Lambda1050 spectroradiometer (Perkin Elmer inc.) was deployed to obtain a continuous ground truth measurement in the interval $400 - 2500\,nm$. Such an instrument deploys two sensors: a Photomultiplier Tube (PMT) for the range $400 - 860\,nm$ and an Indium-Gallium-Arsenide (InGaAS) detector for the range $861 - 2500\,nm$. Therefore, the spectral region of interest of the VNIR-SWIR splicing correction is included in a single sensor (InGaAs) sensitivity range. A total of 175 samples coming from a collection of oil-painted mockups [21] are measured. Such samples possess a level of texture high enough to produce slight differences in BRDF at the pixel level. In evaluating the final result, two properties of the reconstructed spectra are evaluated:

1. Conformity with the spectral shape of the ground truth, evaluated through the usage of Spectral Angle (*SA*) [22],
2. Minimun intervention on the original spectra, measured by means of the root mean square percentage error (*RMSPE*) [23].

The rationale behind the choice of not considering a metric that compares the absolute reflectance values of the ground truth and the VNIR-SWIR spectra resides in the fact that the spectroradiometer averages the measurement over an area, while the highly textural samples possess a high degree of spectral variability that makes the magnitude comparison meaningless at the pixel level. Furthermore, the acquisition geometries of hyperspectral capture and spectroscopy are different.

The proposed method (LOG) is compared against the existing state of the art of splicing correction in spectroscopy. The parabolic correction (PAR) was adapted following the insight of [17] and correcting the last 60 bands of VNIR. The first VNIR wavelength to be corrected is then $785\,nm$, while the juncture point was selected in the middle of the overlap area at $973\,nm$. Although discouraged from usage, we also include the multiplicative correction (MUL), computing the global coefficient as the ratio between the SWIR and VNIR bands at $950\,nm$.

Since the selected correction methods affect a different number of bands, it is necessary to compare the evaluation metrics in turn in the relative intervals of influence, as reported on the x axis of Figure 3. The results of *SA* between the spliced spectra and the ground truth are however affected by the *SA* that exists between the original disconnected spectra and the ground truth. For this reason, it is decided to analyze the difference of SA (ΔSA) in Figure 3c. Figure 3a highlights how the multiplicative correction introduces a lot of unnecessary perturbations, while the parabolic and logistic corrections achieve fairly similar results. From Figure 3b and 3c it is possible to notice that the proposed logistic correction produces more faithful spectral shapes consistently.

Figure 4 highlights the limitations of the multiplicative and parabolic corrections in some specific cases. When considering

Fig. 3. Mean values for *RMSPE* **(a)**, *SA* **(b)**, and ΔSA **(c)** in different intervals of affected spectral bands: logistic (LOG), parabolic (PAR), and multiplicative (MUL).

a global coefficient for the whole spectrum, the relative magnitude perturbation that is introduced is highly impacting when the energy of the spectrum is low, as Figure 4a depicts. On the other hand, the parabolic correction shows a rapidly increasing perturbation in spectral shape as the spectral discrepancy also increases (Figures 4b and 4c), confirming the previous observation of [7]. The proposed logistic correction is proved to be more stable to such specific cases that have anyway a likely occurrence, as depicted by the frequency histograms of spectral energy at the overlap and relative spectral discrepancy.

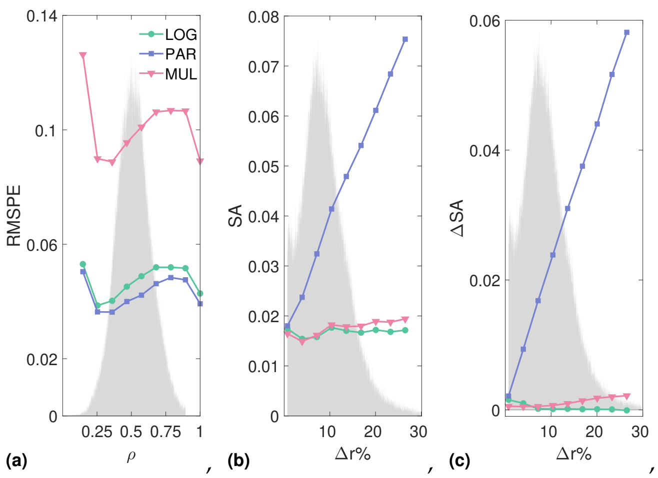

Fig. 4. Behavior of the selected corrections in specific cases of spectral energy **(a)** and spectral discrepancy **(b,c)**. The overlayed histograms (normalized for displaying purposes) illustrate the probability distributions of the events of spectral energy ρ and relative spectral discrepancy $\Delta r\%$.

In summary, we propose a new adaptive splicing correction routine to smoothly connect hyperspectral images that present spectral jumps in correspondence of adjacent spectral sensitivity intervals. The correction is performed in absolute reflectance space and it is adaptive in the sense that the amount of spectral bands affected depends on the magnitude of the initial spectral discrepancy. Advantages against the existing state of the art include better stability in cases of larger spectral discrepancies, which occur more likely in the case of imaging rather than in point spectroscopy. The proposed method presents however a few shortcomings in splicing specific spectral shapes, as we highlight in Figure S2 and Figure S3 in Supplement 1. Therefore, it will be necessary in the future to extend the modeling of splicing correction to account for different levels of spectral complexity.

Funding. Placeholder for funding that will be automatically generated.

Disclosures. The authors declare no conflicts of interest.

Data availability. Data underlying the results presented in this paper are not publicly available at this time but may be obtained from the authors upon reasonable request.

Supplemental document. See Supplement 1 for supporting content. The code for splicing correction on individual spectra and on images can be found at https://github.com/federigr/HyperspectralSplicingCorrection.

REFERENCES

1. J. Sandak, A. Sandak, L. Legan, K. Retko, M. Kavčič, J. Kosel, F. Poohphajai, R. H. Diaz, V. Ponnuchamy, N. Sajinčič *et al.*, Coatings **11**, 244 (2021).
2. A. Siedliska, P. Baranowski, M. Zubik, W. Mazurek, and B. Sosnowska, Postharvest Biol. Technol. **139**, 115 (2018).
3. C. Camino, V. González-Dugo, P. Hernández, J. Sillero, and P. J. Zarco-Tejada, Int. journal applied earth observation geoinformation **70**, 105 (2018).
4. M. Selva, B. Aiazzi, F. Butera, L. Chiarantini, and S. Baronti, IEEE J. selected topics applied earth observations remote sensing **8**, 3008 (2015).
5. J. K. Delaney, J. G. Zeibel, M. Thoury, R. Littleton, M. Palmer, K. M. Morales, E. R. de La Rie, and A. Hoenigswald, Appl. spectroscopy **64**, 584 (2010).
6. M. Danner, M. Locherer, T. Hank, and K. Richter, GFZ Data Serv. (2015).
7. A. Hueni and A. Bialek, IEEE J. Sel. Top. Appl. Earth Obs. Remote. Sens. **10**, 1542 (2017).
8. T. H. Hemmer and T. L. Westphal, Algorithms for Multispectral, Hyperspectral, Ultraspectral Imag. VI **4049**, 249 (2000).
9. D. Benedikovic, L. Virot, G. Aubin, J.-M. Hartmann, F. Amar, X. Le Roux, C. Alonso-Ramos, É. Cassan, D. Marris-Morini, J.-M. Fédéli *et al.*, Nanophotonics **10**, 1059 (2021).
10. B. Jalali and S. Fathpour, J. lightwave technology **24**, 4600 (2006).
11. G. L. Hansen, J. Schmit, and T. Casselman, J. Appl. Phys. **53**, 7099 (1982).
12. W. Dorigo, M. Bachmann, and W. Heldens, User's manual, Ger. Aerosp. Cent. (DLR), Oberpfaffenhofen (2006).
13. D. Beal and M. Eamon, Anal. Spectr. Devices, Inc (2009).
14. R. J. Murphy, S. T. Monteiro, and S. Schneider, IEEE Trans. on Geosci. Remote. Sens. **50**, 3066 (2012).
15. J. A. Curcio and C. C. Petty, JOSA **41**, 302 (1951).
16. F. O. Bartell, E. L. Dereniak, and W. L. Wolfe, Radiat. scattering optical systems **257**, 154 (1981).
17. U. Okyay and S. D. Khan, Photogramm. Eng. & Remote. Sens. **84**, 781 (2018).
18. F. Grillini, J.-B. Thomas, and S. George, Color. Imaging Conf. **2021**, 276 (2021).
19. D. M. Conover, J. K. Delaney, and M. H. Loew, Appl. Phys. A **119**, 1567 (2015).
20. F. Grillini, J.-B. Thomas, and S. George, 2022 12th Workshop on Hyperspectral Imaging Signal Process. Evol. Remote. Sens. (WHISPERS) pp. presented, awaiting proceedings (2022).
21. F. Grillini, J.-B. Thomas, and S. George, Sensors **21**, 2471 (2021).
22. F. A. Kruse, A. Lefkoff, J. Boardman, K. Heidebrecht, A. Shapiro, P. Barloon, and A. Goetz, Remote. sensing environment **44**, 145 (1993).
23. H.-S. Lee and M.-T. Chou, Int. J. Comput. Math. **81**, 781 (2004).

FULL REFERENCES

1. J. Sandak, A. Sandak, L. Legan, K. Retko, M. Kavčič, J. Kosel, F. Poohphajai, R. H. Diaz, V. Ponnuchamy, N. Sajinčič *et al.*, "Nondestructive evaluation of heritage object coatings with four hyperspectral imaging systems," Coatings **11**, 244 (2021).
2. A. Siedliska, P. Baranowski, M. Zubik, W. Mazurek, and B. Sosnowska, "Detection of fungal infections in strawberry fruit by vnir/swir hyperspectral imaging," Postharvest Biol. Technol. **139**, 115–126 (2018).
3. C. Camino, V. González-Dugo, P. Hernández, J. Sillero, and P. J. Zarco-Tejada, "Improved nitrogen retrievals with airborne-derived fluorescence and plant traits quantified from vnir-swir hyperspectral imagery in the context of precision agriculture," Int. journal applied earth observation geoinformation **70**, 105–117 (2018).
4. M. Selva, B. Aiazzi, F. Butera, L. Chiarantini, and S. Baronti, "Hyper-sharpening: A first approach on sim-ga data," IEEE J. selected topics applied earth observations remote sensing **8**, 3008–3024 (2015).
5. J. K. Delaney, J. G. Zeibel, M. Thoury, R. Littleton, M. Palmer, K. M. Morales, E. R. de La Rie, and A. Hoenigswald, "Visible and infrared imaging spectroscopy of picasso's harlequin musician: mapping and identification of artist materials in situ," Appl. spectroscopy **64**, 584–594 (2010).
6. M. Danner, M. Locherer, T. Hank, and K. Richter, "Spectral sampling with the asd fieldspec4," GFZ Data Serv. (2015).
7. A. Hueni and A. Bialek, "Cause, effect, and correction of field spectroradiometer interchannel radiometric steps," IEEE J. Sel. Top. Appl. Earth Obs. Remote. Sens. **10**, 1542–1551 (2017).
8. T. H. Hemmer and T. L. Westphal, "Lessons learned in the postprocessing of field spectroradiometric data covering the 0.4-2.5-um wavelength region," in *Algorithms for Multispectral, Hyperspectral, and Ultraspectral Imagery VI,* vol. 4049 (SPIE, 2000), pp. 249–260.
9. D. Benedikovic, L. Virot, G. Aubin, J.-M. Hartmann, F. Amar, X. Le Roux, C. Alonso-Ramos, É. Cassan, D. Marris-Morini, J.-M. Fédéli *et al.*, "Silicon–germanium receivers for short-wave-infrared optoelectronics and communications," Nanophotonics **10**, 1059–1079 (2021).
10. B. Jalali and S. Fathpour, "Silicon photonics," J. lightwave technology **24**, 4600–4615 (2006).
11. G. L. Hansen, J. Schmit, and T. Casselman, "Energy gap versus alloy composition and temperature in hg1- x cd x te," J. Appl. Phys. **53**, 7099–7101 (1982).
12. W. Dorigo, M. Bachmann, and W. Heldens, "As toolbox and processing of field spectra," User's manual, Ger. Aerosp. Cent. (DLR), Oberpfaffenhofen (2006).
13. D. Beal and M. Eamon, "Preliminary results of testing and a proposal for radiometric error correction using dynamic, parabolic linear transformations of "stepped" data," Anal. Spectr. Devices, Inc (2009).
14. R. J. Murphy, S. T. Monteiro, and S. Schneider, "Evaluating classification techniques for mapping vertical geology using field-based hyperspectral sensors," IEEE Trans. on Geosci. Remote. Sens. **50**, 3066–3080 (2012).
15. J. A. Curcio and C. C. Petty, "The near infrared absorption spectrum of liquid water," JOSA **41**, 302–304 (1951).
16. F. O. Bartell, E. L. Dereniak, and W. L. Wolfe, "The theory and measurement of bidirectional reflectance distribution function (brdf) and bidirectional transmittance distribution function (btdf)," in *Radiation scattering in optical systems,* vol. 257 (SPIE, 1981), pp. 154–160.
17. U. Okyay and S. D. Khan, "Spatial co-registration and spectral concatenation of panoramic ground-based hyperspectral images," Photogramm. Eng. & Remote. Sens. **84**, 781–790 (2018).
18. F. Grillini, J.-B. Thomas, and S. George, "Radiometric spectral fusion of vnir and swir hyperspectral cameras," in *Color and Imaging Conference,* vol. 2021 (Society for Imaging Science and Technology, 2021), pp. 276–281.
19. D. M. Conover, J. K. Delaney, and M. H. Loew, "Automatic registration and mosaicking of technical images of Old Master paintings," Appl. Phys. A **119**, 1567–1575 (2015).
20. F. Grillini, J.-B. Thomas, and S. George, "Hyperspectral vnir-swir image registration: do not throw away those overlapping low snr bands," in *2022 12th Workshop on Hyperspectral Imaging and Signal Processing: Evolution in Remote Sensing (WHISPERS),* (IEEE, 2022), pp. presented, awaiting proceedings.
21. F. Grillini, J.-B. Thomas, and S. George, "Comparison of imaging models for spectral unmixing in oil painting," Sensors **21**, 2471 (2021).
22. F. A. Kruse, A. Lefkoff, J. Boardman, K. Heidebrecht, A. Shapiro, P. Barloon, and A. Goetz, "The spectral image processing system (sips)—interactive visualization and analysis of imaging spectrometer data," Remote. sensing environment **44**, 145–163 (1993).
23. H.-S. Lee and M.-T. Chou, "Fuzzy forecasting based on fuzzy time series," Int. J. Comput. Math. **81**, 781–789 (2004).